Relaxation-time enhancement in the heavy-fermion systems $CePd_3$ and UPt_3

A. M. Awasthi, W. P. Beyermann,* J. P. Carini, and G. Grüner

Department of Physics and Solid State Science Center, University of California, Los Angeles, California 90024

(Received 13 September 1988)

The frequency dependence of the electrical conductivity was measured at microwave- and millimeter-wave frequencies in the heavy-fermion materials $CePd_3$ and UPt_3. Although the conductivity is independent of the frequency at high temperatures, a substantial deviation from the dc conductivity develops in the low-temperature, "coherent" regime. The observed dependence on frequency agrees with a Drude expression $\sigma_1(\omega) = \sigma_{dc}/(1 + \omega^2\tau^{*2})$, incorporating a renormalized relaxation time τ^* typically around 10^{-12} s. From τ^* and the measured σ_{dc}, the renormalized plasma frequency, $\omega_p^* = (\sigma_{dc}/\epsilon_0\tau^*)^{1/2}$ is evaluated. By comparison of ω_p^* with the plasma frequency obtained at optical frequencies, where renormalization effects do not occur, an enhanced mass is extracted. Similar results are found by comparison of ω_p^* with the linear specific-heat coefficient. The enhanced relaxation time is approximately given by the expression $\tau^*/\tau = m^*/m_e$, where τ and m_e refer to the unrenormalized quantities, supporting the conjectures of Varma and Fukuyama, and the theoretical models advanced by Millis and co-workers, Auerbach and co-workers, and Coleman. An internally consistent analysis of $\sigma(\omega)$ in terms of an enhanced relaxation time also suggests that a frequency-dependent density of states does not play a dominant role in the frequency-dependent response measured in the millimeter-wave spectral range. Possible Fermi-liquid and low-energy density-of-state contributions to the frequency-dependent conductivity are also discussed.

I. INTRODUCTION

The consequences of electron-electron interactions are usually described in terms of enhancement effects.[1-7] Various thermodynamic quantities, such as the electronic specific heat and magnetic susceptibility, are extremely large in many intermetallic compounds which include rare-earth atoms,[8-10] and the Wilson ratio, given by χ/γ at low temperatures, is generally close to unity.[7] Enhanced effects only occur at low temperatures below a so-called characteristic temperature T_c. Depending on the model used to account for the various experiments, T_c is usually associated with either a Kondo temperature or a spin-fluctuation temperature and is related to the correlation narrowed bandwidth. At temperatures above T_c, correlation effects are not important. Here we do not make a distinction among the different characteristic temperatures such as those suggested[11] for $CePd_3$ since the differences are not significant for our results. Strong correlations also play an important role in the transport properties. In the low-temperature region, the temperature-dependent dc resistivity is given by

$$\rho_{dc} = \rho_{dc}(T=0) + AT^2 , \qquad (1)$$

where $\rho_{dc}(T=0)$ is the residual resistivity. The notion of heavy fermions is usually used to discuss the thermal and magnetic properties which are described by a narrow band near the Fermi level ε_F,[7] and the various thermodynamic quantities together with the coefficient A are generally described in terms of an enhanced effective mass m^*.[4,5] Both γ and χ are proportional to m^* while $A \sim m^{*2}$. Therefore γ^2 is proportional to A, as observed in a variety of materials with substantial enhancement

effects.[12] Both the thermoelectric power[13,14] and Hall effect[15-17] are anomalous, and together give evidence for a narrow resonance at ε_F associated with a correlated state below T_c.

In this paper we present experimental results concerning another aspect of the correlations: the enhancement of the transport relaxation time τ^* which enters into the relevant expressions for the electrical conductivity. It has been recently suggested, that the dc conductivity σ_{dc} is not influenced by correlation effects because the enhancement of the relaxation time cancels the enhancement of the effective mass in the relations for electrical transport, and

$$\tau^*/\tau = m^*/m_e , \qquad (2)$$

where τ and m_e are the unenhanced relaxation time and free-electron mass. The preceding expression follows from treatments of the problem within the framework of Fermi-liquid theory. For strong correlations the enhancement of the relaxation time can be substantial. If a material has a low-temperature dc conductivity comparable to the room-temperature conductivity of copper (on the order of 1 $\mu\Omega^{-1}cm^{-1}$), an effective-mass enhancement of $m^*/m_e \sim 200$ leads to a $\tau^* \sim 3 \times 10^{-15}$ s $\times 200 = 6 \times 10^{-13}$ s (provided the two materials have similar carrier concentrations). The relaxation rate $(2\pi\tau^*)^{-1}$ is then in the millimeter-wave spectral range. This implies a strongly frequency-dependent Drude-type response with a roll-off occurring at millimeter-wave frequencies. Fermi-liquid theory, which leads to a dc resistivity given by Eq. (1) similarly predicts a frequency-dependent relaxation time with the frequency-dependent

effects becoming more important for larger effective masses.[18]

Strong correlations also lead to correlation narrowed bandwidths, and the typical width of the many-body resonance around ϵ_F is given qualitatively by $B^* = (m_b / m^*)B_{\text{bare}}$, where B_{bare} is the unrenormalized conduction electron bandwidth. Assuming $B_{\text{bare}} \sim 1$ eV, a value of $m^*/m_b \sim 10^2$ yields $B^* = \hbar \omega^* \sim 10$ meV, which corresponds to $\omega^* \sim 10^{13}$ s^{-1}. This frequency is comparable to the relaxation rate estimated earlier. Narrow bandwidths have been inferred from various experiments, such as the thermoelectric power[13,14] or tunneling[19] in several materials with large effective masses. A strongly frequency-dependent density of states $D(\epsilon)$ is also expected to affect the measured frequency-dependent response by introducing an energy-dependent relaxation time $\tau(\epsilon)$ in addition to the frequency dependence of $D(\epsilon)$. Although correlation effects are important at low energies ($\epsilon \lesssim B^*$), renormalization does not occur at higher energies; hence the optical properties reflect the unrenormalized parameter like the band mass m_b.

We conducted conductivity measurements up to 150 GHz, (corresponding to $\omega^{-1} \sim 10^{-12}$ s) in two compounds: $CePd_3$, and UPt_3. In the first compound, $CePd_3$, the mass enhancement is on the order of[20] $m^*/m_e \sim 40$, and the correlation-narrowed bandwidth is approximately 20 meV which is significantly above our upper measurement frequency. In UPt_3 the mass enhancement is substantially larger[21]: $m^*/m_e \sim 280$; however, this is due in part to the relatively small bandwidth, which produces a band mass approximately 1 order of magnitude larger than the free-electron mass. Also, an enhanced effective mass has been found in UPt_3 by de Haas–van Alphen measurements.[22]

The paper is organized as follows. In Sec. II we describe the experimental technique and the main results. Section III contains a brief overview of the relevant theories and discusses our results including a comparison with the optical measurements. Finally, conclusions are summarized in Sec. IV.

II. EXPERIMENTAL TECHNIQUES AND RESULTS

A. Experimental methods and analysis

Surface impedance measurements were employed to evaluate the frequency-dependent conductivity in the millimeter-wave spectral range. Because the method has not been used in the past to measure the transport properties of heavy-fermion materials, we describe the principle behind the techniques, the experimental apparatus, and the procedures for collecting and analyzing the data.

The complex quantity called the surface impedance, which has both a resistive R_s and a reactive X_s component, is defined as

$$Z_s \equiv R_s + iX_s \equiv \left[\frac{E_x}{H_y}\right]_{z=0} = \frac{i\mu_0\omega}{H_y}\int_0^\infty H_y dz , \quad (3)$$

where the final equality follows from Maxwell's equations. E_x and H_y are the electric and magnetic fields, and

μ_0 is the permeability of free space. The coordinate system is chosen so that x and y axes lie in the plane of the material, and the z axis points into the surface. From this definition it is evident that the impedance is determined by the parallel fields at the surface.

We want to relate the surface impedance defined earlier to the cavity parameters that are measured. Initially consider a cavity of volume V enclosed by an infinitely conducting surface. When excited by an oscillating electromagnetic wave, the cavity will resonate at a frequency ω_0 determined by the boundary conditions for the fields. For a perfectly conducting surface, the tangential component of the electric field and the normal component of the magnetic induction must be zero. With these constraints imposed, only certain eigenfrequencies are allowed for a given set of cavity dimensions. Also, since there are no losses in this system, the quality factor Q_u is infinite. Now imagine the cavity with a finite impedance. The fields penetrate the walls as the effective shielding by the induced currents is reduced. The resulting change in energy alters the resonant frequency, and the Ohmic losses in the surface produce a finite unloaded Q_u.

This phenomenon can be described quantitatively using the perturbation equation[23,24]

$$\frac{\omega^* - \omega_0^*}{\omega^*} = -\frac{\int_{\Delta V}[(\epsilon - \epsilon_0)\mathbf{E}_0^* \cdot \mathbf{E} + (\mu - \mu_0)\mathbf{H}_0^* \cdot \mathbf{H}]dv}{4U_{\text{total}}} . \quad (4)$$

Here the subscripted symbols (e.g., ϵ_0, μ_0, E_0, H_0, and ω_0^*) are the unperturbed quantities pertaining to an ideal cavity whose boundaries have a zero surface impedance; the quantities lacking subscripts refer to the perturbed cavity resulting from a nonzero Z_s. The integral is over the additional volume acquired when the fields are allowed to penetrate into the walls because of the finite surface impedance, and U_{total} is the total energy stored in the cavity. At places where the electric field is parallel to the surface, the unperturbed field at the boundary is zero, while on the surfaces, where it is perpendicular, the free charges completely screen out the interior electric fields. In either case, there is no electric field contribution to the integral.

Recalling that the unperturbed Q_u is infinite, the complex resonant frequencies on the left-hand side are

$$\omega^* = \omega + i\frac{\omega}{2Q_u} \text{ and } \omega_0^* = \omega_0 . \quad (5)$$

Substituting these expressions into Eq. (4) and dropping second-order terms yields an integral expression approximately proportional to the increase in magnetic energy due to a finite impedance. Assuming the surface material is nonmagnetic, the final result is

$$\frac{\omega - \omega_0}{\omega} + i\frac{1}{2Q_u} = -\frac{\mu_0}{4U_{\text{total}}}\int_{\Delta V}\mathbf{H}_0^* \cdot \mathbf{H}dV$$

$$= i\frac{Z_s}{4\omega U_{\text{total}}}\int_s |H_0|^2 ds , \quad (6)$$

where Eq. (3) was used to introduce Z_s into the calculation.

The above relation can be separated into its real and imaginary parts. Expressed more conveniently,

$$\Delta\omega = \omega - \omega_0 = -\sum_j \frac{1}{2}\gamma_j X_{sj} \; , \tag{7a}$$

$$\Gamma = \frac{\omega_0}{Q_u} = \sum_j \gamma_j R_{sj} \; , \tag{7b}$$

where the terms on the right are summed over all the surfaces enclosing the resonant cavity, and R_{sj} and X_{sj} are, respectively, the resistance and reactance of the jth surface. The coefficient γ_j, referred to as the resonator constant, is defined by

$$\gamma_j \equiv \frac{\int_{s_j} |H_0|^2 ds}{2U_{\text{total}}} \; . \tag{8}$$

Notice that the integral in the numerator extends only over the area of the jth surface. Each bounding surface has associated with it a resonator constant that depends on the cavity dimensions. With expression (8), we are able to relate measurable parameters such as $\Delta\omega$ and Γ to sample-dependent quantities like R_s and X_s.

We are ultimately interested in measuring σ and ϵ; therefore, these quantities must be expressed in terms of the surface impedance. It is assumed that locality holds, and the induced current at a given point is linearly determined by the applied field at the same position. This is valid as long as the field does not vary appreciably over a mean path. However, the relationship between the field and current is not constrained to be instantaneous in time. At sufficiently high frequencies, the inertia of the electrons leads to relaxation effects, and the current at a particular time may depend on the electric field at an earlier time. With these considerations in mind, the current is proportional to the applied field (i.e., Ohm's law holds), and the proportionality constant may be complex.

The surface impedance was defined by Eq. (3), and it can be rewritten in terms of the complex propagation constant as

$$Z_s = \frac{\mu_0\omega}{k^*} \; . \tag{9}$$

The propagation constant can be found from the wave equation that results by combining Maxwell's equations, and we have

$$(k^*)^2 = \mu_0\epsilon_0\omega^2\left[\epsilon_1 - \frac{i\sigma_1}{\epsilon_0\omega}\right] \; . \tag{10}$$

Taking the square root of both sides yields

$$ik^* = \alpha + i\beta \; ,$$

$$\alpha = \frac{\omega}{c}\left[\frac{1}{2}\right]^{1/2}\left\{\left[\epsilon_1^2 + \left[\frac{\sigma_1}{\epsilon_0\omega}\right]^2\right]^{1/2} - \epsilon_1\right\}^{1/2} , \tag{11}$$

$$\beta = \frac{\omega}{c}\left[\frac{1}{2}\right]^{1/2}\left\{\left[\epsilon_1^2 + \left[\frac{\sigma_1}{\epsilon_0\omega}\right]^2\right]^{1/2} + \epsilon_1\right\}^{1/2} ,$$

where σ_1 and ϵ_1 refer to the real parts of the conductivity and dielectric constant. Throughout this paper we will use the notation $\sigma = \sigma_1 + i\sigma_2$ and $\epsilon = i\sigma/\epsilon_0\omega$. Substituting into Eq. (9), the impedance is

$$Z_s = \frac{\mu_0\omega}{\alpha^2 + \beta^2}(\beta + i\alpha) \; . \tag{12}$$

This general expression, which includes relaxation effects, is rather complicated, and we will next explore several limiting cases.

First assume that σ_1 is much greater than $\epsilon_0\epsilon_1\omega$. Then $\alpha = \beta$, and the impedance becomes

$$Z_s = \frac{1}{\delta_{\text{cl}}\sigma_1}(1+i) = \left[\frac{\mu_0\omega}{2\sigma_1}\right]^{1/2}(1+i) \; . \tag{13}$$

δ_{cl} is of course the classical skin depth, and this limit is usually denoted as the classical or normal skin effect region. Here the magnitudes of both the real and imaginary impedances are equal.

The opposite possibility is to have σ_1 much less than $\epsilon_0\epsilon_1\omega$. In this case, referred to as the transmission region,

$$\alpha = 0 \text{ and } \beta = \frac{\omega}{c}\sqrt{\epsilon_1} \; . \tag{14}$$

For the impedance we have

$$Z_s = \left[\frac{\mu_0}{\epsilon_0\epsilon_1}\right]^{1/2} , \tag{15}$$

which is just the impedance of free-space reduced by the index of refraction for the medium.

In principle, the measurement of R_s and X_s allows one to evaluate both $\sigma_1(\omega)$ and $\sigma_2(\omega)$ [or alternatively, $\epsilon(\omega)$] through Eqs. (11) and (12). Unfortunately, the absolute measurement of X_s is generally difficult. We have assumed therefore that, at high temperatures, the resistivity is that of a simple metal and Eq. (13) applies. This leads to a normalization for X_s, and subsequently, the temperature dependence and magnitude of X_s can be evaluated.

All the experiments performed in this paper utilized cylindrical cavities that resonate in the TE$_{011}$ mode, where the electric field has only components perpendicular to the cylindrical axis. The fields vary one half cycle in the radial and longitudinal directions, but are independent of the angular variable. There are two reasons for selecting this mode. First, it has a very high Q, increasing the sensitivity of the measurement, and second, the currents do not flow between the cylindrical body and the end plates, where the existence of a poor joint could lead to excess loss and a lower Q. Also in surface impedance measurements, where the sample is clamped onto the end of the cavity, an uncertain contact has little effect on the measurement. Despite its desirability, the TE$_{011}$ mode has a couple of disadvantages. Because the currents flow in a circular direction, anisotropic surface impendance experiments are limited. Another drawback is that the TE$_{011}$ mode is degenerate with the TM$_{111}$ mode, and steps must be taken in the construction to split this degeneracy since the relations connecting the cavity and sample parameters rely on the existence of a unique field configuration inside the cavity. Mode splitting was ac-

complished by strategically machining ledges on each side of the cavity body where the fields for the TM_{111} mode are present. The energy stored in each mode is no longer the same, shifting their resonant frequencies and resulting in the described separation. There is negligible degradation of the desired mode provided the ledge is small enough so that the perturbation upsets only the unwanted mode. Once a mode, a frequency, and the ratio between the diameter and height of the cavity, d/h, are selected, the cavity dimensions can be determined. Care should be exercised in choosing the ratio d/h because it affects the cavity Q. It is desirable to have as large a Q as possible since this enhances the determination of the resonant width and position, and the maximum Q value occurs when the ratio is equal to one. The density of modes, however, increases as the ratio is decreased and becomes fairly large in the neighborhood where Q reaches its maximum value. In order to avoid the undesirable interference between two adjacent modes, a compromise was struck by selecting a ratio of 1.5 for the cavities.

Consideration is given in designing the coupling holes for the cavities. To excite a particular mode, the hole or iris must connect similar field patterns in both the waveguide and cavity, (i.e., the electric and magnetic field vectors should point in the same direction). This means that the position and relative orientation of the waveguide, cavity, and iris are important.

The degree of coupling is also important. The strongest coupling occurs when a hole is located at 0.47 times the cavity radius where the radial magnetic field of the TE_{011} mode is a maximum, and when the hole is also centered with respect to the waveguide, which is sometimes a problem because the input and output waveguides in a transmission configuration may overlap. When transmission waveguides overlap, the iris is placed at a distance equal to the mean of the two optimum positions. The energy radiated through the coupling hole is minimized by operating the cavity in an undercoupled configuration. There are several ways of changing the coupling to achieve an undercoupled cavity. Reducing the diameter of the iris, increasing the length of the coupling hole (i.e., the thickness of the coupling plate), and moving the iris to a less optimal location are all effective at altering the coupling.

A surface impedence experiment is performed by clamping a sample, which has a flat polished surface, to the bottom of the cavity and measuring the resonant parameters as a function of temperature. After replacing the sample with a smooth copper end plate, the sample-out resonance is recorded at the same temperatures. By adding up the contributions of each loss mechanism existing in the cavity, the total energy dissipated is found and expressed in terms of a loaded quality factor Q_l. From the resonance width, Q_l is determined, and we have for the sample-in and -out runs, respectively,

$$\frac{1}{Q_{ls}} = \frac{1}{Q_r} + \frac{1}{Q_{us}} + \frac{1}{Q_{ms}} ,$$

$$\frac{1}{Q_{lo}} = \frac{1}{Q_r} + \frac{1}{Q_{uo}} + \frac{1}{Q_{mo}} .$$

(16)

In these relations, Q_r is the energy lost through the coupling holes; Q_{us} and Q_{uo} are the unloaded Q's which are affected by the presence of the sample; Q_{ms} and Q_{mo} represent any unknown loss contributions not contained in the other terms.

Subtracting these expressions and using Eq. (7b), the change in resonance width caused by the sample is

$$\Delta\omega - \Delta\omega_0 = \gamma(R_s - R_{cu}) ,$$

(17)

where Q_{ms} and Q_{mo} are assumed to cancel out. Here the sample and copper end plates are taken to have the same surface area and equivalent resonator constants γ. For the end plate of a cavity in the TE_{011} mode, the resonator constant calculated using Eq. (8) is

$$\gamma = \frac{2}{\mu_0 h^3} \left[\frac{c\pi}{\omega} \right]^2 .$$

(18)

In this expression c is the speed of light. Also observe that in Eq. (17), the sample's resistance is measured relative to that of copper. Care must be exercised in calculating the copper's contribution, especially since copper is in the anomalous limit at these frequencies and at lower temperatures. Consequently, the measured temperature dependence of R_s is probably more reliable than the absolute values.

After a cavity is constructed, external circuitry must be supplied to collect the resonant width and position. Either a transmission or reflection configuration can be employed and both are illustrated in Fig. 1.
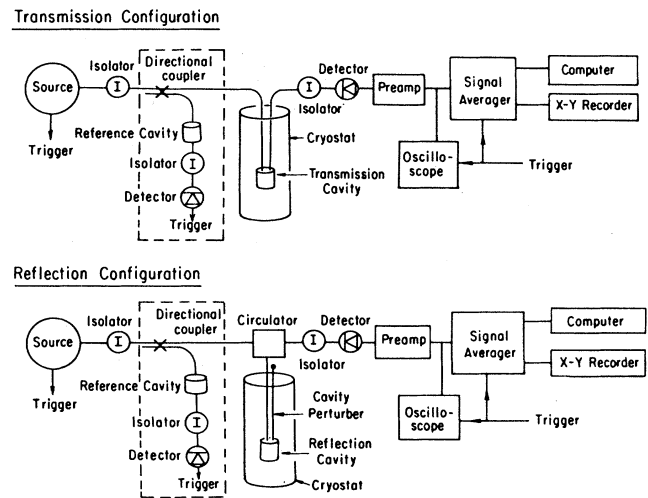

FIG. 1. Experimental components and their arrangement needed to perform cavity measurements. Both a transmission and a reflection configuration are displayed. The apparatus enclosed inside the dashed box is optional and used to supply a reference resonance for either a trigger or calibration point. Sometimes attenuators and/or phase shifters are inserted at various locations to reduce the effects from spurious reflections in the apparatus (e.g., the vacuum window and waveguide joints).

The 102 and 150 GHz cavities utilized a transmission configuration. In this arrangement, a HP 8350B sweep oscillator drives an Impatt source which furnishes the microwave power. With standard rectangular waveguides, this source is connected to the input part of the cavity and the output part goes to a crystal broadband detector. The detector and source are matched to the transmission lines with ferrite isolators. An optional reference arm consisting of a 10 dB coupler, reference cavity, and a detector, may also be included between the source and cavity providing a reference resonance to act as a trigger or calibration point. All the waveguide components, hardware, and the Impatt source, were manufactured by Hughes Aircraft Company. By modulating the frequency, the resonance was monitored in real time using an oscilloscope and recorded with a Nicolet 370 or −1170 signal averager. The averager could be triggered by either an output on the source or a reference cavity. Since the cavity was way undercoupled, the signal was very weak and had to be amplified using an EG&G model 113 preamplifier before averaging. A thousand or so sweeps gave an adequate signal-to-noise ratio. After being recorded, the resonance was transferred to an IBM-PC where its width and relative position were calculated.

To perform the measurements at different temperatures, the cavity was placed in a stainless-steel liquid-helium cryostat, and a Lakeshore temperature controller allowed data to be taken from 1.2 to 300 K. The cavity was isolated from the bath with a copper can which contained a partial atmosphere of helium exchange gas, and to reduce the heat leak, the waveguides descending into the cryostat were stainless steel. Unfortunately, the large attenuation inherent in stainless steel degrades the signal-to-noise ratio, and for this reason the probe was kept as short as possible. The distance between the top plate of the probe and the cavity was 35.5 cm.

A reflection arrangement was used with the 35 GHz cavity. The apparatus and procedures are similar to those described for the transmission configuration with a few modifications. Instead of separate input and output transmission lines, a single waveguide connects the cavity to a circulator which directs power from the source to the cavity and then the returning reflection from the cavity back to the detector. In a transmission configuration, no power reaches the detector unless the cavity is resonating. However, in a reflection configuration, all the power is reflected from the cavity and detected except what is absorbed at resonance. To obtain the net resonant absorption, the background must be subtracted off, and, for an ideal system this is no problem because the background constitutes a flat baseline as the frequency is varied. When there are spurious reflections from discontinuities in the waveguide that interfere with the returning signal, the baseline is no longer constant. If the signal is highly attenuated because stainless-steel waveguides and undercoupled cavities are used, distinguishing the resonance from the irregular baseline becomes difficult. An accurate determination of the width and position can only be achieved by shifting the resonance with respect to the baseline and then subtracting off the background. A perturbing mechanism was designed which inserts a quartz rod into the cavity moving the resonant frequency and leaving undisturbed background, and the signal averager facilitates the subtraction of perturbed from the unperturbed traces. Unfortunately at higher frequencies, the baselines become so distorted that the sources of the baseline subtraction diminishes, and for this reason the transmission cavities were preferred at 102 and 150 GHz.

Even in a transmission configuration, reflections in the lines can be a problem and conspire to alter the resonance. Also the external circuitry such as the source, detector, or even the waveguide components may be slightly frequency dependent, distorting the resonance. In our case, however, these effects were negligible.

To verify the experimental technique, we measured a sample of $TiBe_2$ which is a normal metal and should not show any frequency dependence in the millimeter-wave spectral range. From Eq. (13), R_s^2/ω is proportional to $\rho_{dc} = 1/\sigma_{dc}$ if $\sigma_1 \gg \epsilon_0\epsilon_1\omega$. In Fig. 2, the temperature dependences of R_s^2/ω and ρ_{dc} are displayed indicating no significant frequency dependence at 102 GHz as expected. The microwave data was normalized at room temperature to the dc value.

B. Experimental results

During the initial steps of the experiments, the surface resistance R_s was measured both in $CePd_3$ and in UPt_3. The experimental results, plotted as R_s^2/ω, are displayed, together with the measured dc resistivity in Figs. 3 and 4. The reason for this representation is that for a Drude metal with $1/\tau \gg \omega$, $R_s^2/\omega \propto \rho_{dc}$ and gives the resistivity of the material. Consequently, when the quantity agrees with ρ_{dc}, it implies, that the conductivity is frequency independent in the measured spectral range. This is the case for $CePd_3$ above the resistivity maximum ($T \approx 124$
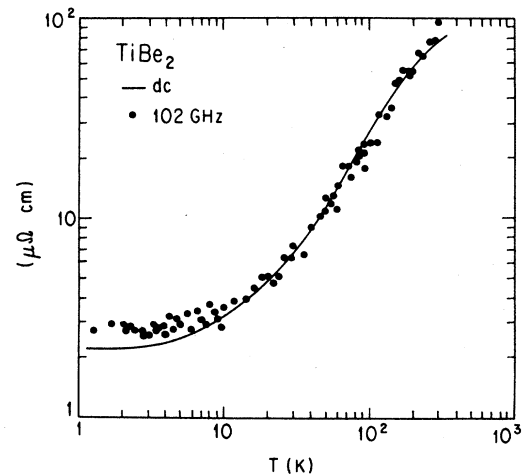

FIG. 2. The temperature dependence of the dc resistivity and $2R_s^2/\mu_0\omega$ for $TiBe_2$. The microwave conductivity was measured at 102 GHz and normalized to the dc value at room temperature.
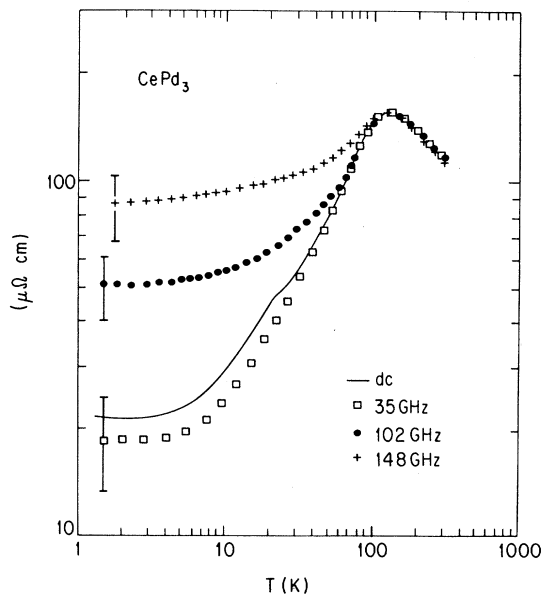
FIG. 3. Temperature dependence of $2R_s^2/\mu_0\omega$ at various frequencies and ρ_{dc} for $CePd_3$. All the high-frequency data are normalized to the dc resistivity at $T = 100$ K.
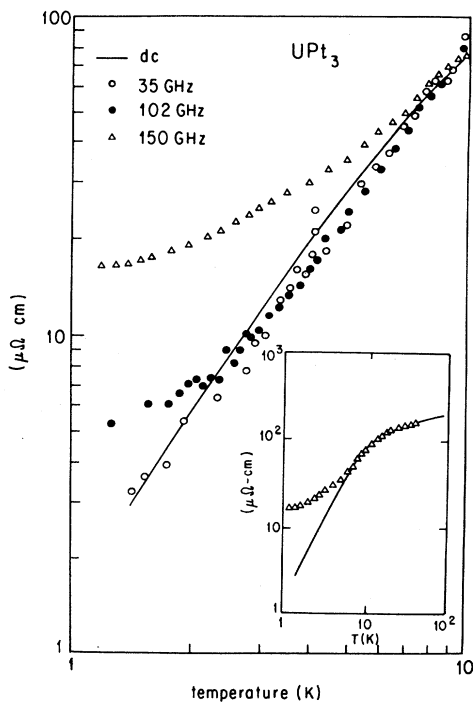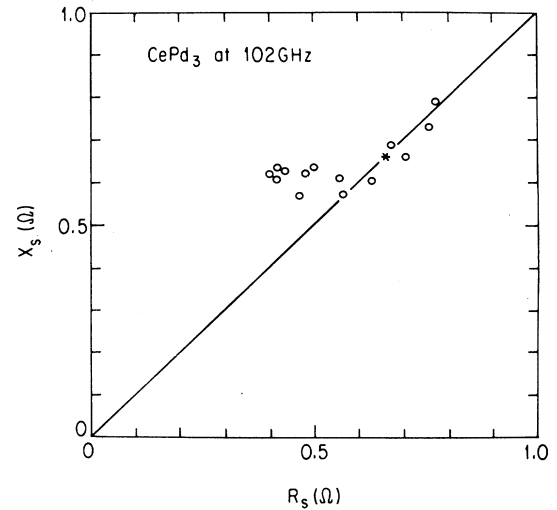

FIG. 5. The real component vs the imaginary component of the surface impedance at 102 GHz for $CePd_3$. The different points were taken at different temperatures and represent the changing relaxation time. The data were normalized at room temperature which is indicated by the asterisk, and the deviation from the diagonal line occurs when $\sigma_1 \sim \epsilon_0\epsilon_1\omega$.

K), and also for UPt_3 at temperatures above approximately 10 K.

As discussed earlier, Eq. (13) implies $R_s = X_s$ when the relaxation time is short in the Drude model and $\sigma_1 \gg \epsilon_0\epsilon_1\omega$. We have therefore plotted R_s versus X_s for data obtained at various temperatures in Figs. 5 and 6. The higher temperature data are in the upper right part

FIG. 4. The dc resistivity and $2R_s^2/\mu_0\omega$ as a function of temperature for UPt_3. The microwave data at various frequencies were normalized at $T = 10$ K. In the insert the high-temperature behavior is displayed where there is no frequency dependence.
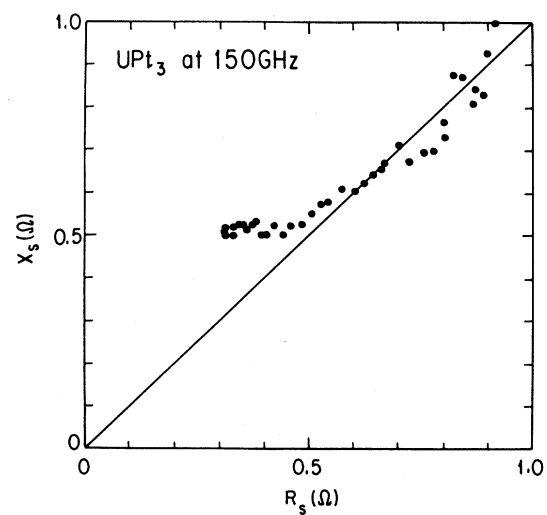

FIG. 6. The real component vs the imaginary component of the surface impedance for UPt_3. The measurement was performed at 150 GHz and normalized at $T = 10$ K.
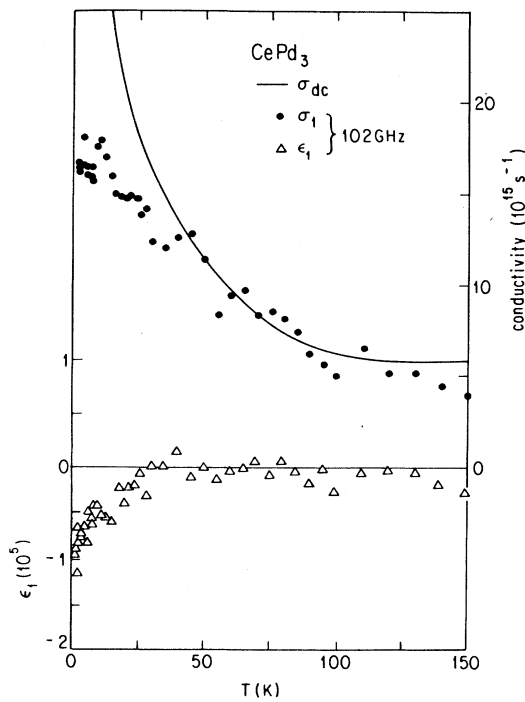
FIG. 7. The temperature dependence of the real components of the conductivity and dielectric constant measured at 102 GHz for $CePd_3$.
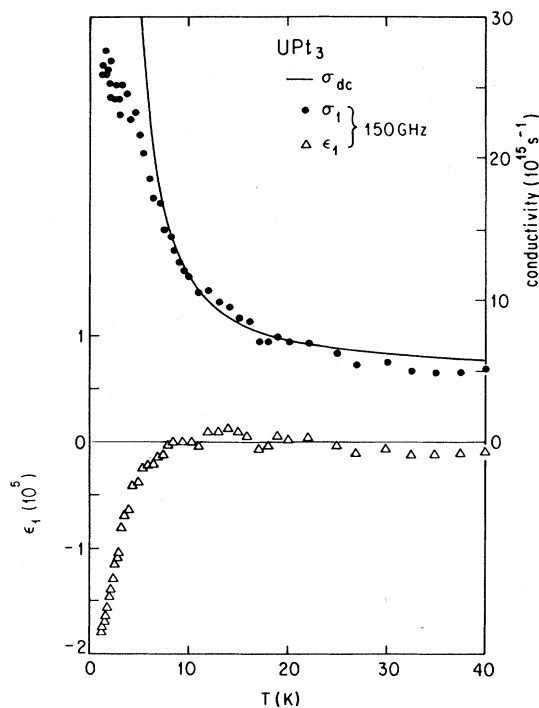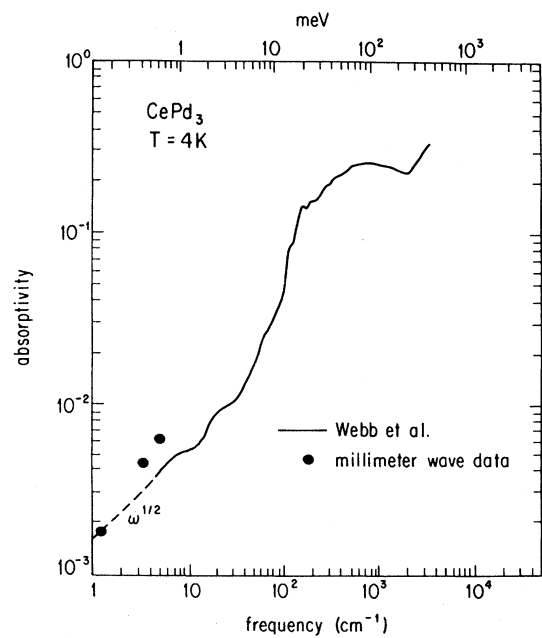

FIG. 9. The absorptivity measured in $CePd_3$ at $T = 4$ K. The solid line represents the optical data, and the microwave data are indicated by the solid dots. The dashed line is the low-frequency result expected from the Hagen-Rubens relation.

FIG. 8. The real conductivity and dielectric constant vs temperature for UPt_3. These data were taken at 150 GHz.
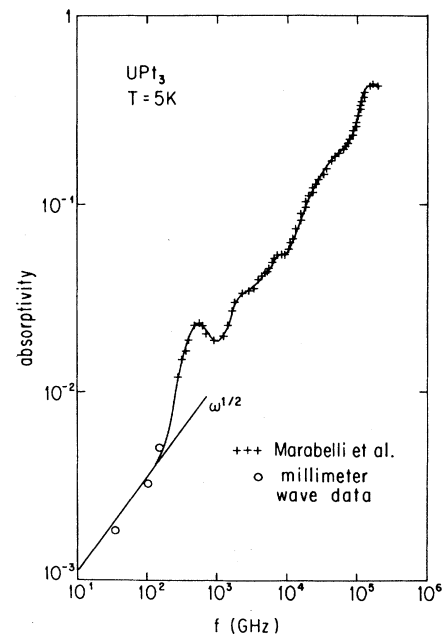

FIG. 10. The absorptivity measured in UPt_3 at $T = 5$ K showing both the optical and millimeter-wave data. Also displayed is the low-frequency result expected from the Hagen-Rubens relation.

of the figures, and the implications of Eq. (13) are satisfied for both materials. Deviations from this behavior are evident at low temperatures where $R_s < X_s$ suggesting that both $\sigma_1(\omega)$ and $\epsilon_1(\omega)$ make important contributions to the surface impedance. In this regime σ is frequency dependent and both R_s and X_s must be measured to perform a full analysis. Figures 7 and 8 show the conductivity and dielectric constant as a function of temperature obtained from a measurement of R_s and X_s for CePd$_3$ at $\omega/2\pi = 102$ GHz and for UPt$_3$ at $\omega/2\pi = 150$ GHz.

We have also compared our surface impedance measurements with the optical measurements of Webb et al.[25] for CePd$_3$, and Travaglini et al.[26] for UPt$_3$. In both cases, the reflectivity R was measured, allowing for the evaluation of the absorptivity $1-R$. This is shown in Figs. 9 and 10 together with our surface impedance results. Note that in the low-frequency limit, the Hagen-Rubens relation[27,28]

$$1 - R = \left[\frac{8\epsilon_0 \omega}{\sigma_1} \right]^{1/2}, \tag{19}$$

should hold, and this is directly related to the surface impedance given by Eq. (13).

While, in general, there is a good overall agreement, we find important differences between our measured values and those inferred from the optical data. Neither in CePd$_3$ nor in UPt$_3$ do we find that $1-R$ or Z_s is proportional to $\omega^{1/2}$ as expected from a frequency-independent conductivity which has been used to extrapolate the optical data to zero frequency. This has important consequences on the analysis of our experimental results presented in the next section.

III. DISCUSSION OF RELEVANT THEORIES AND OUR RESULTS

A. Theories of a frequency-dependent response

First, we will discuss the various theories concerning the frequency-dependent conductivity in strongly correlated metals and the techniques for extracting an effective mass from the measured frequency-dependent response.

Unlike the single impurity problem, the dc resistivity vanishes at $T=0$ for a periodic lattice, and the low-temperature resistivity is determined by impurity scattering. Calculations[5] find a low-energy relaxation rate that contains both a contribution from impurity scattering and a frequency-dependent term representing the scattering of electrons off the slave bosons. At low frequencies, impurity scattering dominates, and the conductivity is given by a renormalized Drude expression of the form

$$\sigma(\omega) = \frac{ne^2\tau^*}{m^*} \frac{1}{1+\omega^2\tau_i^{*2}}, \tag{20}$$

where n equals the sum of the electrons in the conduction and $4f$ bands (i.e., $n = n_c + n_f$). m^* is the effective mass, and τ_i^* is a renormalized relaxation time determined by impurity scattering. The dc conductivity is not affected

by electron-electron interactions, and Fermi-liquid theory leads to Eq. (2).

One may also define a renormalized plasma frequency which is given by[29]

$$\omega_p^* = \left[\frac{\sigma_{dc}}{\epsilon_0 \tau_i^*} \right]^{1/2} = \left[\frac{ne^2}{\epsilon_0 m^*} \right]^{1/2}. \tag{21}$$

Above a crossover frequency ω_{co}, frequency-dependent scattering becomes important, and the conductivity levels off at a very low value given by

$$\sigma_1(\omega) = \frac{ne^2}{m_b} \frac{1}{B_{bare}}, \tag{22}$$

which is frequency independent. The crossover frequency separating the two regimes is

$$\omega_{co} \simeq \left[\frac{NB_{bare}}{\hbar\tau_i} \right]^{1/2} \frac{m_b}{m^*}. \tag{23}$$

The degeneracy of the f orbital equals N and is of order unity. With $\tau_i \sim 3 \times 10^{-15}$ s, $B_{bare} \sim 1$ eV, and $m^*/m_b \sim 100$, we estimate $f_{co} = \omega_{co}/2\pi \sim 1$ THz which is significantly above our upper measurement frequency. This calculation has only qualitative significance, however, since it neglects complications such as the Fermi surface geometry and Umklapp processes. Also, energy scales smaller than the above value were suggested by various experiments.

When either the frequency or temperature are larger than the renormalized Fermi energy associated with the ground state, B^* (the analog of the Kondo temperature in the single impurity case), unrenormalized response is expected. Finally, the preceding conclusions hold provided $B^*\tau_i^* \gg 1$ which is probably satisfied for CePd$_3$ and UPt$_3$.

In principle, the optical conductivity for $\omega \gg \omega_{co}$ is characterized by an unrenormalized plasma frequency

$$\omega_p = \left[\frac{\sigma_{dc}}{\epsilon_0 \tau} \right]^{1/2} = \left[\frac{n_c e^2}{\epsilon_0 m_b} \right]^{1/2}, \tag{24}$$

where m_b is the unrenormalized band mass, and n_c equals the number of conduction electrons without the $4f$-band contribution. Band structure effects may play an important role in determining the plasma frequency ω_p, which can be regarded as an average of the plasma frequencies characterizing the optical response at various orientations and frequencies. The plasma frequencies were measured in CePd$_3$ and UPt$_3$ by optical methods; these values are collected in Table I.

The two plasma frequencies can be combined to give

$$\frac{\omega_p}{\omega_p^*} = \left[\frac{m^*}{m_b} \right]^{1/2} \left[\frac{n_c}{n} \right]^{1/2}, \tag{25}$$

and this quantity is related to the ratio of the enhanced effective mass to the band mass. Ideally, a measurement of $\sigma(\omega)$ over a broad frequency range allows the evaluation of m^*/m_b, without any additional assumption about the number of electrons or k_F. In contrast, several as-

TABLE I. Summary of the measured and calculated quantities for $CePd_3$ and UPt_3. The calculated parameters were extracted from a comparison of the low- and high-frequency conductivity data. All the entries were determined at $T = 1.5$ K.

	τ^* $(10^{-12}$ s$)$	ω_p^* $(10^{15}$ s$^{-1})$	ω_p $(10^{15}$ s$^{-1})$	m^*/m_b
$CePd_3$	1.9	0.53	3.5[a]	44
UPt_3	3.24	1.03	3.8[b]	14

[a]Reference 25.
[b]Reference 26.

sumptions must be made when extracting the effective mass from the thermodynamic quantities.

We note that the renormalized plasma frequency defined in Eq. (21) is different from the lower plasma frequency where $\epsilon_1(\omega)$ goes from negative to positive with increasing frequency. This latter quantity not only reflects the renormalized mass, but also a renormalized Coulomb interaction and is given by[29,30]

$$\omega_{p1}^* = [6(1 + n_f/n_c)]^{1/2}T^* , \qquad (26)$$

where T^* is a renormalized Fermi temperature. In Fig. 11, we sketch both $\sigma_1(\omega)$ and $\epsilon_1(\omega)$ which follows from various theories[4-6] based either on auxiliary-boson $1/N$ expansion or a functional-integral treatment of the Anderson Hamiltonian with the parameters discussed earlier. Also evident is the peak in the conductivity result-
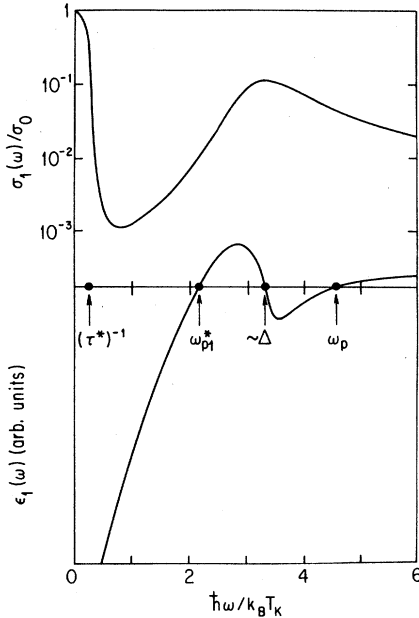

FIG. 11. The frequency dependence of the real components of the conductivity and the dielectric constant expected for a typical heavy-fermion compound in the coherent state. These results follow from calculations by Millis et al., Auebrach et al., and Coleman.

ing from interband transitions across the hybridization gap Δ.

In the range where the dc resistivity is strongly temperature dependent and is given by Eq. (1), the scattering of electrons off fluctuations is important. The prefactor appearing in this expression scales as (B^*) which is a result of phase space arguments, and it is consequently proportional to m^{*2}. The validity of the relation $A \sim \gamma^2$ was demonstrated for a broad range of heavy-fermion systems.[12] In the above limit, the frequency-dependent conductivity has been calculated at frequencies both above and below ω_{co}. For low frequencies

$$\rho(\omega, T) = \frac{m}{ne^2} \left[\frac{m^*}{m} \frac{\hbar\omega^2}{\epsilon_F} + \frac{m^*}{m} \frac{\alpha\pi^2 k^2 T^2}{\hbar\epsilon_F} \right] , \qquad (27)$$

with the coefficient α close to one. In Eq. (27) the ω-dependent response comes from the ω dependence of the fluctuations, and its origin is distinctly different from the ω-dependent conductivity that follows from the Drude form. In principle, the ω-dependent response can be evaluated by incorporating a frequency-dependent scattering time into a Kubo expression. However, for our purposes, in the low-frequency limit the two leading terms of the ω-dependent response, one given by the Drude expression without an ω-dependent τ^*, and the other given by the ω-dependent scattering rate, are combined to yield

$$\rho_{total} = \frac{m}{ne^2} \left[\frac{1}{\tau} + \left[\frac{m^*}{m} \right]^2 \frac{\pi^2 k^2 T^2}{\hbar\epsilon_F} \right.$$
$$\left. + \omega^2 \left[\frac{m^*}{m} \right]^2 \left[\tau + \frac{\hbar}{\epsilon_F} \right] \right] , \qquad (28)$$

where it has been assumed that $\epsilon_F^* = (m/m^*)\epsilon_F$, i.e., that the Fermi energy is renormalized by the same amount as the effective mass. In the preceding equation the first and second terms give the impurity and fluctuation contributions to the resistivity assuming Mathiessen's rule. The ω-dependent contribution is given by

$$\rho(\omega) = \frac{m\omega^2}{ne^2} \left[\frac{m^*}{m} \right]^2 (\tau + \hbar/\epsilon_F) \qquad (29)$$

It is evident from the preceding expression, that the two contributions—Drude and $\tau(\omega)$—are comparable if $\tau \sim \hbar/\epsilon_F$. However, as τ is given by the time between successive scatterings which lead to the resistivity and

$\hbar/\varepsilon_F$ is the characteristic time for transfer of electrons between neighboring lattice sites, one expects to find for the majority of cases (as long as $l > a$, the lattice constant) $\tau \gg \hbar/\varepsilon_F$, and $\rho(\omega)$ is dominated by the Drude term.

The overall features of the frequency-dependent resistivity are in agreement with the discussion given earlier. In all cases the low-temperature resistivity increases with increasing frequency around 100 GHz. This frequency is roughly the same as $1/\tau^*$ for a large effective mass [see Eq. (2)] and the deviation occurs in the temperature region where ρ_{dc} is strongly temperature dependent; the ω-dependent and T-dependent conductivities are comparable when $\hbar\omega \sim kT$, as suggested by expression Eq. (28). However, the Drude relaxational contribution to the observed ω-dependent response should dominate at low temperatures where the mean free path is significantly larger than the lattice constant. Consequently, we first analyze the experimental results in terms of a renormalized Drude theory, and then discuss the temperature dependences.

B. Evaluation of the components of the frequency-dependent conductivity

As discussed earlier, if $\sigma_1 \gg \sigma_2$, the surface resistance is directly related to σ_1 through Eq. (13), and σ_1 can be evaluated from the measured R_s. This situation is appropriate for CePd$_3$, see Fig. 7, and $\sigma_1(\omega)$ evaluated from R_s is displayed in Fig. 12 as the function of frequency at $T = 4$ K and $T = 300$ K. Also shown in the figure is the
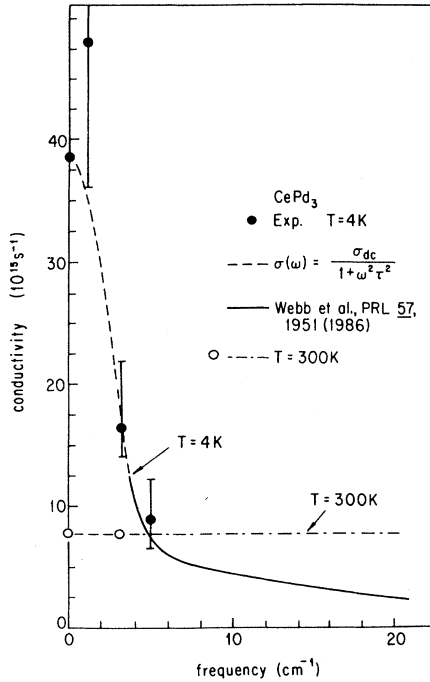

FIG. 12. Frequency-dependent conductivity at $T = 4$ K and $T = 300$ K for CePd$_3$. The solid line is the optical data from Webb et al.

data by Webb et al.[25] illustrating the approximate agreement between the two experiments. It is evident, that σ_1 is approximately independent of frequency at room temperature, but a zero frequency narrow resonance develops in the low-temperature, coherent regime. The dotted line in Fig. 12 is a renormalized Drude expression, Eq. (20), with a renormalized relaxation time $\tau^* = 2 \times 10^{-12}$ s. This parameter will be used later to evaluate a renormalized plasma frequency and renormalized mass.

The dielectric constant $\epsilon_1(\omega)$ [or alternatively, $\sigma_2(\omega)$] is smaller than what would be expected from a Drude expression

$$\sigma_D(\omega) = \frac{\sigma_{DC}}{1 - i\omega\tau^*} , \tag{30}$$

without taking into account the high-energy contribution to $\sigma(\omega)$. Assuming that the Drude and high-energy contributions to σ_2 are additive,

$$\sigma_2(\omega) = \sigma_{D2}(\omega) - \epsilon_0 \epsilon_{IB} \omega , \tag{31}$$

where $\epsilon_{IB}(\omega)$ represents the dielectric constant coming from the high-frequency, presumably interband, processes. For CePd$_3$, the optical data for σ_1 by Webb et al.[25] shows a pronounced peak at $\Delta = 56.8$ THz, and this translates to a low-frequency dielectric constant

$$\epsilon_{ib} = 1 + \frac{1}{\epsilon_0} \frac{ne^2}{m\Delta^2} = 100 , \tag{32}$$

with $n = 4 \times 10^{27}/\text{m}^3$. The Drude term with the previously determined τ^* and σ_{dc} gives

$$\sigma_{D2}(\omega) = 3.77 \times 10^5 \ \Omega^{-1}\text{m}^{-1} , \tag{33}$$

at 102 GHz, and the sum of the two contributions yields a value for $\sigma_2(\omega)$ in close agreement with the experimentally measured σ_2, see Fig. 7.

Rewriting expression (20) as

$$C = \frac{\rho(\omega) - \rho_{dc}}{\rho_{dc}} = 1 + \omega^2 \tau^{*2} , \tag{34}$$

C is evaluated and plotted versus ω^2 in Fig. 13 for CePd$_3$. Within experimental accuracy, Eq. (34) is obeyed for temperatures up to approximately 60 K, suggesting that a Drude expression is appropriate to describe the experimental results obtained at low temperatures.

For UPt$_3$ the condition $\sigma_1 \gg \sigma_2$ does not hold, and both X_s and R_s must be used in order to evaluate the two components of the conductivity. Due to experimental difficulties, we were able to measure both components only at one frequency, $f = 150$ GHz. Consequently, certain assumptions were made in order to extract σ_1 and σ_2 at different frequencies.

We assumed that σ_2 is given in UPt$_3$ by Eq. (31), and used this equation, together with σ_2 measured at 150 GHz to evaluate ϵ_{ib}. With the second term in the right-hand side of Eq. (31) known, the relation between R_s and σ_1 can be derived, and subsequently σ_1 was evaluated from the measured R_s value. The results of this analysis are displayed in Fig. 14 together with the optical data by Marabelli et al.[26] At $T = 300$ K, our analysis described
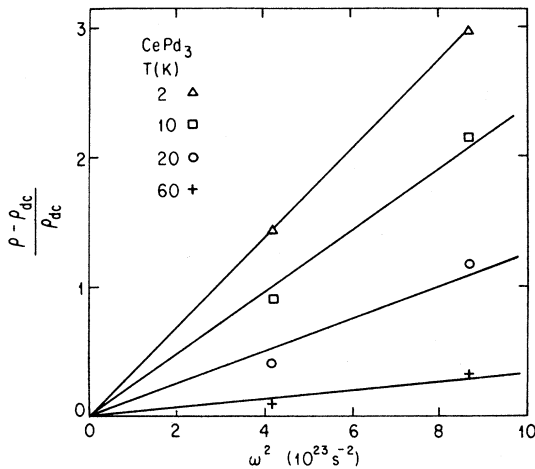
FIG. 13. Frequency dependence of $\rho(\omega) - \rho_{dc}/\rho_{dc}$ at various temperatures for CePd$_3$. The solid lines are fits to the Drude expression, Eq. (34).

earlier has not been performed as at this temperature, $\sigma_2 \ll \sigma_1$ and R_s gives σ_1 directly. As for CePd$_3$, the conductivity is independent of frequency at high temperatures with the strongly frequency-dependent narrow resonance appearing only at low temperatures. The dotted line in Fig. 12 is the fit to the renormalized Drude expression, Eq. (20), giving a relaxation time $\tau^* = 2 \times 10^{-12}$ s.
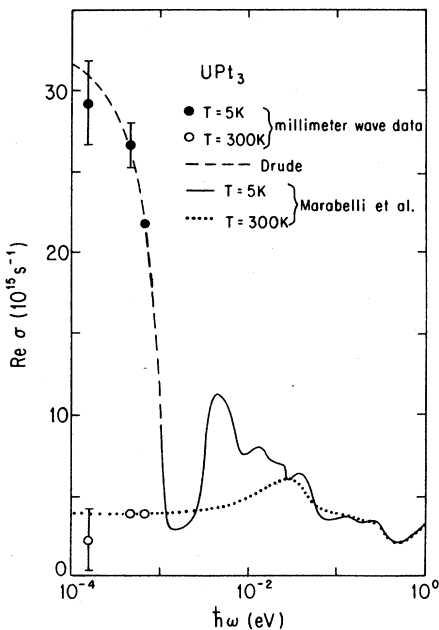
Data taken at different temperatures can be used to extract the temperature dependence of the relaxation time for both compounds, and this is displayed in Figs. 15 and 16, along with the temperature dependence of the dc resistivity. The temperature dependences of $(\tau^*)^{-1}$ and ρ_{dc} are the same, and our experimental accuracy is not sufficient to comment on the deviations observed at low temperatures.

C. Evaluation of enhancement effects

The renormalized parameters, which are extracted from the low-frequency conductivity measurements, can be used in combination with other experimental data to evaluate a renormalized effective mass within the framework of simple models. One route is to compare the low-frequency data to the high-frequency optical experiments since renormalization effects occur only below a crossover frequency ω_{co} given by Eq. (23). Because the bare parameters measured at $\omega > \omega_{co}$ reflect the actual band structure, such an analysis leads to an enhancement with respect to the actual average band mass of the material in question. The analysis is also subject to ambiguities associated with anisotropy effects, multiple bands, etc. An alternative analysis can be performed by comparing the low-frequency optical data with specific-heat results, noting that both sample the low-energy excitations of the coherent state. Using a free-electron expression for σ_1 (i.e., a simple Drude formula) and a specific heat coefficient, an enhancement with respect to the free-electron mass is obtained. This approach has the advan-
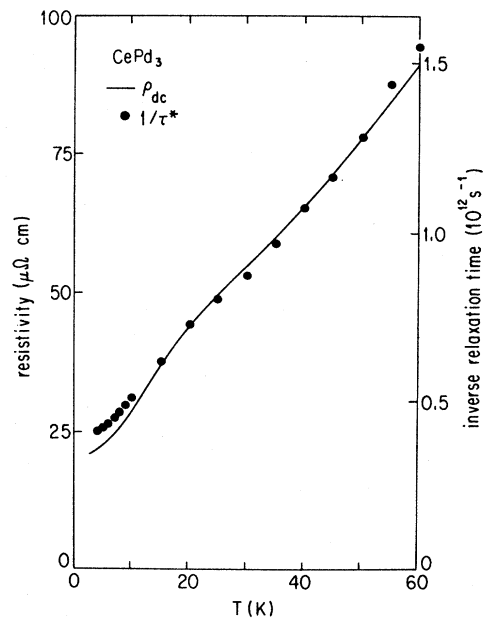

FIG. 14. The real component of the conductivity as a function of frequency for UPt$_3$ at $T = 5$ K and $T = 300$ K. The optical data are from Marabelli et al.

FIG. 15. ρ_{dc} and $1/\tau^*$ vs temperature in CePd$_3$. The similar temperature dependence of these two quantities indicates that n/m^* is independent of temperature in this range.
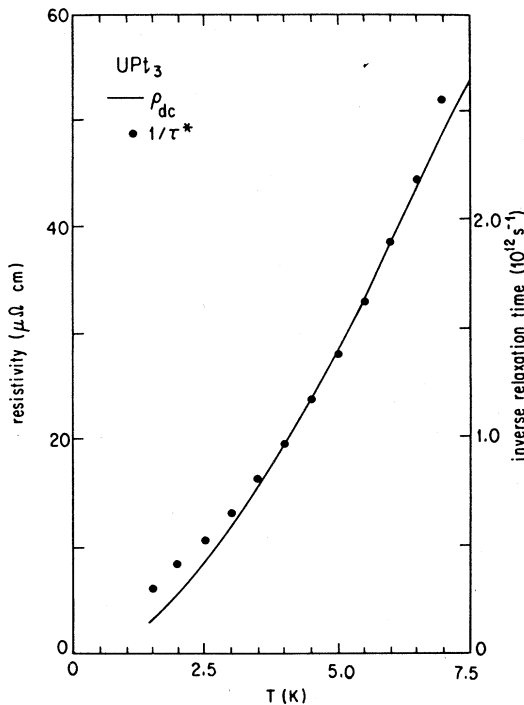
FIG. 16. ρ_{dc} and $1/\tau^*$ at various temperatures in UPt$_3$.

in the high-temperature region to calculate the enhancement. At room temperature,[31] $\omega_p \tau = 12$ for UPt$_3$, and with a residual dc resistivity ratio of 74, an unrenormalized relaxation time is obtained which is $1/\tau = 4.3 \times 10^{12}$ s^{-1} at $T = 1.5$ K. From this the enhancement of the mass is $m^*/m_b = \tau^*/\tau \approx 14$, in exact agreement with that derived by comparing the plasma frequencies.

The enhancement factor m^*/m_b refers to the enhanced effective mass in relation to the band mass, which can be significantly larger than the free-electron mass m_e. In CePd$_3$ the plasma frequency suggests a band mass approximately between $1m_e$ and $2m_e$. Consequently, in this material m^*/m_b is expected to be close to m^*/m_e. In contrast, the conduction band in UPt$_3$ is believed to be heavy, and various band-structure calculations lead to a m_b which is between $17m_e$ and $23m_e$.[32] As a result of the band structure, the total enhancement of the effective mass $m^*/m_e \sim 14 \times 20 = 280$, and it is this value which is probably measured in thermodynamic experiments.

2. Enhancement effects from low-frequency optics and specific heat

While the preceding analysis is appealing because the strength of correlation effects was extracted on the basis of the frequency-dependent conductivity alone, it suffers from ambiguities mainly associated with complicated band-structure effects which determine the unrenormalized plasma frequency and optical relaxation time. An alternative analysis, which compares only parameters which are sensitive to low-energy fluctuations, can also be performed. The specific heat is

$$\gamma = \frac{1}{3} \left[\frac{k_B}{\hbar} \right]^2 (3\pi^2 n)^{1/3} m^* V_m , \qquad (35)$$

for an isotropic free-electron band where V_m is the molar volume. Combining the preceding expression with ω_p^* given by Eq. (21), two parameters m^* and n can be extracted. This analysis avoids difficulties associated with a complicated energy-dependent density of states since both τ^* and γ are determined from experiments which sample the density of states within the same energy range. Note, that 5 K corresponds to approximately 100 GHz, and a specific heat measured at this temperature samples a thermal energy range $k_B T$ comparable to our frequency range. An important caveat in this alternative analysis is that thermodynamic and transport enhancements must be determined by the same electrons. The results of this analysis are included in Table II for comparison to the other quantities. Included in the table is the linear specific-heat coefficient γ taken from the literature and used in the calculation, the renormalized plasma frequency, the density of electrons expressed in terms of the Fermi wavevector k_F for a free-electron model [i.e., $k_F = (3\pi^2 n)^{1/3}$], the valence (number of electrons per formula unit) associated with k_F, and the mass enhancement relative to the free-electron mass m^*/m_e. The effective mass m^* agrees favorably with mass enhancements derived from the low- and high-frequency conductivity data

tage that electrons, within the same energy range of the Fermi surface, are involved in both experimental probes; however, it breaks down if different bands are associated with the enhancements of the specific heat and transport.

1. Enhancement effects from optical properties

As discussed earlier, the optical properties, measured at frequencies above ω_{co} defined in Eq. (23) are not affected by renormalized effects and can be used to evaluate an unrenormalized plasma frequency ω_p given by Eq. (24). Recent optical experiments,[25,26,31] performed from infrared to visible frequencies cover the spectral range which exceeds ω_{co}. Therefore, ω_p obtained by these methods can be compared with the renormalized plasma frequency ω_p^* to extract an enhanced effective mass relative to the band mass m^*/m_b using Eq. (25). We expect that the Pd and Pt bands are nearly full in CePd$_3$ and in UPt$_3$. Hence, the situation is complicated concerning n_c and n_f. Even though the number of conduction electrons and $4f$ electrons is not known, $n_c \sim n_{tot}$ is assumed in the calculation.

The renormalized relaxation time τ^*, renormalized plasma frequency ω_p^*, optical plasma frequency ω_p, and mass enhancement m^*/m_b, are all collected in Table I. These quantities, with the exception of ω_p, were all evaluated at the lowest measurement temperature $T = 1.5$ K.

One can also use the relaxation times measured at millimeter-wave $(\hbar\omega < B^*)$ frequencies in the low-temperature region and at optical $(\hbar\omega > B^*)$ frequencies

TABLE II. Results from the analysis based on a comparison of the low-frequency conductivity data with the specific-heat data. The linear specific-heat coefficients γ, obtained from the literature, were taken at the temperatures where the relaxation times were determined.

	γ (mJ/mol K^2)	ω_p^* (10^{15} s^{-1})	k_{F_1} (Å^{-1})	Valence[a]	m^*/m_e
CePd$_3$	40[b]	0.53	0.464	0.24	38
UPt$_3$	420[c]	1.03	1.398	3.19	277

[a]Electrons per formula unit.
[b]Reference 8.
[c]Reference 9.

and this suggests that a one band model is appropriate to account for the various properties of these materials. A similar conclusion has been reached by comparing the specific heat and magnetic susceptibility to the coefficient A of the temperature-dependent resistivity which appears in Eq. (1).

IV. CONCLUSIONS

In this paper we reported frequency-dependent transport measurements in the millimeter-wave spectral range in two heavy-fermion materials CePd$_3$, and UPt$_3$. The conductivity is strongly frequency dependent in both compounds at low temperatures in the so-called "coherent" regime. We have analyzed the observed conductivity in terms of a renormalized Drude relaxation with a renormalized relaxation time τ^*. Such analysis can be used to extract a renormalized plasma frequency ω_p^*, which is significantly smaller than ω_p measured at optical frequencies. The observation of two plasma frequencies is in agreement with models for the heavy-fermion materials, and was used to extract a mass enhancement. Alternatively, the effective mass can be determined from quantities which characterize the low-energy fluctuations such as ω_p^* and specific-heat coefficient γ. In CePd$_3$ both approaches lead to similar enhancements, suggesting that a single band description which determines both the transport and thermodynamic properties is appropriate.

In UPt$_3$ we obtain an enhancement over the band mass $m^*/m_b = 14$, while the enhancement over the free-electron mass $m^*/m_e = 277$. This then suggests that the band mass m_b is approximately 1 order of magnitude larger than the free-electron mass. The preceding values are in excellent agreement with other estimations and measurements of the effective mass. Band-structure calculations give $m_b \sim 20 m_e$[32], while de Haas–van Alphen

experiments[22] observe a mass enhancement $m^*/m_b < 80$ for all the bands examined.

The success of the analysis for giving mass enhancements in semiquantitative agreement with those obtained from the thermodynamic quantities suggests that our analysis in terms of a renormalized Drude theory is appropriate for these compounds, and the frequency dependence of the relaxation time (as suggested by the Fermi-liquid approach) is negligible.

Several unresolved questions remain, however, and these are related to band-structure effects which determine the band mass and the optical properties over a broad energy range. Such uncertainties are most important in UPt$_3$ which has a fairly anisotropic crystal structure with a large band mass and a complicated density of states. Also, a strongly energy-dependent density of states on a scale of 1 meV or less has been inferred from various experiments, and such effects are expected to strongly influence the ω-dependent low-temperature response.

These uncertainties can be clarified by performing experiments on other heavy-fermion systems with both large and moderate mass enhancements and also by measurements on alloys where the relaxation can be modified without significantly influencing the strength of electron-electron interactions.

ACKNOWLEDGMENTS

*Present address: Los Alamos National Laboratory, Los Alamos, NM 87544.
[1]H. Fukuyama, *Theory of Heavy Fermions and Valence Fluctuations,* edited by T. Kasuya and T. Saso (Springer-Verlag, Berlin, 1985).
[2]C. M. Varma, *Theory of Heavy Fermions and Valence Fluctuations,* edited by T. Kasuya and T. Saso (Springer-Verlag, Berlin, 1985).

[3]C. M. Varma, Phys. Rev. Lett. **55**, 2723 (1985).
[4]A. Auerbach and K. Levin, Phys. Rev. Lett. **57**, 877 (1986).
[5]A. J. Millis and P. A. Lee, Phys. Rev. B **35**, 3394 (1987).
[6]P. Coleman, Phys. Rev. Lett. **59**, 1026 (1987).
[7]P. A. Lee, T. M. Rice, J. W. Serene, L. J. Sham, and J. W. Wilkins, Comments Cond. Mat. Phys. **12**, 99 (1986).
[8]J. M. Lawrence, P. S. Riseborough, and R. D. Parks, Rep. Prog. Phys. **44**, 1 (1981).

[9]G. R. Stewart, Rev. Mod. Phys. **56**, 755 (1984).

[10]H. R. Ott and Z. Frisk, *Handbook on the Physics and Chemistry of the Actinides*, edited by A. J. Freeman and G. H. Lander (North-Holland, Amsterdam, 1987).

[11]J. M. Lawrence, J. D. Thompson, and Y. Y. Chen, Phys. Rev. Lett. **54**, 2537 (1985).

[12]A. Auerbach and K. Levin, Phys. Rev. B **34**, 3524 (1986).

[13]F. Steglich, U. Rauchschwalbe, U. Gottwick, H. M. Mayer, G. Sparn, N. Grewe, U. Poppe, and J. J. M. Franse, J. Appl. Phys. **57**, 3054 (1985).

[14]H. Sthioul, D. Jaccard, and J. Sierro, *Valence Instabilities*, edited by P. Wachter and H. Boppart (North-Holland, Amsterdam, 1982).

[15]J. Schoenes and J. J. Franse, Phys. Rev. B **33**, 5138 (1986).

[16]E. Cattaneo, J. Magn. Magn. Mater. **47&48**, 529 (1985).

[17]A. Fert, P. Pureur, A. Hamzic, and J. P. Kappler, Phys. Rev. B **32**, 7003 (1985).

[18]R. N. Gurzhi, Zh. Eksp. Teor. Fiz. **35**, 965 (1958) [Sov. Phys.—JETP **35**, 673 (1959)].

[19]M. Moser, P. Wachter, J. J. M. Franse, G. P. Meisner, and E. Walker, J. Magn. Magn. Mater. **54 – 57**, 373 (1986).

[20]T. Mihalisin, P. Scoborea, and J. W. Ward, Phys. Rev. Lett. **46**, 862 (1981).

[21]A. de Visser, A. Menovsky, and J. J. M. Franse, J. Magn. Magn. Mater. **63&64**, 365 (1987).

[22]L. Taillefer, R. Newbury, G. G. Lonzarich, Z. Fisk, and J. L. Smith, J. Magn. Magn. Mater. **63&64**, 372 (1987).

[23]J. Müller, Hochfrequenztech. Elektroakust. **54**, 157 (1939).

[24]J. C. Slater, *Microwave Electronics* (Van Nostrand Reinhold, New York, 1950).

[25]B. C. Webb, A. J. Sievers, and T. Mihalisin, Phys. Rev. Lett. **57**, 1951 (1986).

[26]F. Marabelli, G. Travaglini, P. Wachter, and J. J. M. Franse, Solid State Commun. **59**, 381 (1986).

[27]J. M. Ziman, *Principles of the Theory of Solids* (Cambridge, London, 1972), p. 278.

[28]F. Wooten, *Optical Properties of Solids* (Academic, New York, 1972), p. 95.

[29]A. J. Millis, M. Lavagna, and P. A. Lee, Phys. Rev. B **36**, 864 (1987).

[30]P. Fulde, J. Keller, G. Zwichnagl, Solid State Phys. **41**, 1 (1988).

[31]P. C. Eklund, M. H. Yang, A. Rao, E. T. Arakawa, and D. G. Hinks, Bull. Am. Phys. Soc. **32**, 719 (1987).

[32]P. Strange and B. L. Gyorffy, Physica **130B**, 41 (1985); A. M. Boring, R. C. Albers, F. M. Mueller, and D. D. Koelling, *ibid.* **130B**, 171 (1985); T. Oguchi and A. J. Freeman, J. Magn. Magn. Mater. **52**, 174 (1985); C. S. Wang, H. Krakauer, and W. E. Pickett, Physica **135B**, 34 (1985).